Nuclear Inst. and Methods in Physics Research, A 940 (2019) 274–282

Contents lists available at ScienceDirect

Nuclear Inst. and Methods in Physics Research, A

journal homepage: www.elsevier.com/locate/nima

Design, optimization and performance evaluation of BM-PET: A simulation study

Peyman Sheikhzadeh [a,b,c], Hamid Sabet [d], Hossein Ghadiri [b,c], Parham Geramifar [e], Pardis Ghafarian [f,g], Mohammad Reza Ay [b,c,*]

[a] Department of Nuclear Medicine, Vali-Asr Hospital, Tehran University of Medical Sciences, Tehran, Iran
[b] Department of Medical Physics and Biomedical Engineering, Tehran University of Medical Science, Tehran, Iran
[c] Research Center for Molecular and Cellular Imaging, Tehran University of Medical Sciences, Tehran, Iran
[d] Department of Radiology, Massachusetts General Hospital, Harvard Medical School, Boston, MA, USA
[e] Research Center for Nuclear Medicine, Shariati Hospital, Tehran University of Medical Sciences, Tehran, Iran
[f] Chronic Respiratory Diseases Research Center, National Research Institute of Tuberculosis and Lung Diseases (NRITLD), Shahid Beheshti University of Medical Sciences, Tehran, Iran
[g] PET/CT and Cyclotron Center, Masih Daneshvari Hospital, Shahid Beheshti University of Medical Sciences, Tehran, Iran

ARTICLE INFO

Keywords:
Brain-dedicated PET
Monte Carlo simulation
Optimization
Image quality enhancement

ABSTRACT

Introduction: The aim of this work is to report on modeling and evaluation of potential performance characteristics of Brain Mapping PET (BM-PET) which is under development at our center. BM-PET is based on expansion of our recently developed small animal PET system (Xtrim-PET) and optimize the geometry of its detector system for brain imaging applications.

Methods: We modeled an accurate representation of Xtrim-PET in GATE and after validation of the model, we extended our model to design and optimize the BM-PET scanner followed by defining a cost function and running series evaluation tests in terms of different geometrical, physical and detection parameters. Resolution recovery and attenuation correction techniques were developed and applied to the simulated data. Finally, the performance of the BM-PET system is evaluated and compared with two simulated models of commercially available brain scanners.

Results: The optimized rotating cylindrical BM-PET based on LYSO-SiPM detectors with dimension of 2×2×20 mm^3 resulted in system sensitivity of ˜16 cps/kBq and 2.1 mm FWHM spatial resolution when tested using the NEMA standard. Detection efficiency of BM-PET is 1.2x and 2.1x higher than our simulated NeuroPET and HRRT scanners. The calculated spatial resolution of the BM-PET in rotation mode is approximately 0.8 and 0.2 mm better compared with that of the mentioned scanners.

Conclusion: Optimization of the BM-PET geometry and detector configuration, implementation of scanner rotation/wobbling and utilization of image correction and enhancement techniques, improved the performance of our modeled brain PET and direct us to manufacture of a prototype scanner.

1. Introduction

Design and development of dedicated brain PET scanners has been escalated in the past decade mainly due to high demand for brain studies and the rise of neurological disorders such as Alzheimer's disease. Conventional whole-body PET (WB-PET) scanners however, fall short when high resolution image and high sensitivity is required for those brain studies. Compared with the brain scanners, the longer distance between the detectors and the region of interest in WB-PET resulting in low solid angle and photon non-collinearity is to blame for their limited performance. Among many scanner characteristics for brain-dedicated PET, we believe that the following four features are the most important: (a) High-sensitivity (system sensitivity higher than 10 cps/kBq): for the lowest possible injected activity and dynamic imaging capability for brain functional studies (b) High spatial resolution: to allow accurate metabolism imaging and receptor specifications identification for small structures in brain and accurate measurement of quantitative indices. To reach this capability, we need spatial resolution of 2 mm or less in all 3D field-of-view (FOV) (c) Low manufacturing and imaging cost: to allow widespread use. (d) Multi-modal imaging compatibility: to increase the diagnosis accuracy.

Different designs and geometries candidate for brain scanner have been modeled and studied [1–4]. More compact hemispherical geometry has been recently presented [5] but for lack of opposite detectors,

* Corresponding author at: Department of Medical Physics and Biomedical Engineering, Tehran University of Medical Science, Tehran, Iran
E-mail address: mohammadreza_ay@tums.ac.ir (M.R. Ay).

https://doi.org/10.1016/j.nima.2019.05.083
Received 14 December 2018; Received in revised form 20 May 2019; Accepted 26 May 2019
Available online 13 June 2019
0168-9002/

Table 1
Summary of the Xtrim specification.

Number of detector blocks	10
Crystal type	LYSO
Number of crystals per block	24×24
Crystal pixel size	2×2×10 mm^3
Crystal pixel pitch	2.1×2.1 mm^2
Number of crystal per detector ring	240
Total number of crystals	5760
Ring diameter	180 mm
Bore opening	120 mm
Time window	5–10 ns
Axial field-of-view	50.3 mm
SiPM array	12×12
SiPM pixel size	3×3 mm^2

add-on chin detectors were proposed to cover some of the missed line of responses (LOR) and to prevent data missing [5]. We proposed symmetrical spheroid geometry to have pair opposite detectors and cover LORs [4,6]. However, spherical-based designs using conventional detector designs increases parallax errors in peripheral LORs, degrading quantification in region of interests [7] that needs detectors with depth of interaction (DOI) that adds to the hardware cost. The inherent large gap between detector blocks which degrades image quality especially in peripheral source positions and complexity of scanner manufacturing are other disadvantages of spherical geometry brain PET scanner. We believe that optimized cylindrical scanner can provide higher mean performance and be a still suitable candidate for dedicated brain scanners especially for multi-modal brain systems. Therefore, due to less complexity and higher compatibility with other modalities, we developed the cylindrical model as a high-performance dedicated brain PET system in our center. BrainPET which was an insert for a clinical MR system consisting of LSO:Ce scintillators and magnetically insensitive avalanche photodiodes detectors (APD) was the first human brain tomograph for simultaneous (functional) PET and MR imaging that produced high quality images in one bed position [8]. NeuroPET scanner is a cylindrical brain PET/CT scanner recently manufactured using silicon photomultiplier (SiPM) and LYSO:Ce scintillator which can provide a sensitivity of 11.7 kcps/MBq and transverse resolution of 3.2 mm [9–11]. Magnetic Resonance (MR) insertable cylindrical brain PET with Geiger-mode avalanche photodiode (GAPD) and LYSO:Ce scintillators was one of the other attempts for new brain scanners development. Sensitivity of 0.3% and the spatial resolution of 3.1 mm were reported for the mentioned scanner [12]. More recently, TRIMAGE as a tri-modal simultaneous PET/MR/EEG brain scanner based on full-ring cylindrical geometry, was developed to address the need for dedicated-brain PET systems for the investigation of psychiatric diseases biomarkers in the human brain [13,14]. In this work, we outline the design and optimization of a brain PET scanner we are developing in our center and describe GATE Monte-Carlo model of the envisaged PET detector system, followed by design optimization as well as image enhancement methods for artifact reduction.

2. Methods

2.1. Validation of Monte Carlo model

The design of our brain PET scanner is based on expansion of our recently developed small animal PET, Xtrim [15]. The Xtrim preclinical PET system is equipped with pixelated LYSO:Ce coupled to SiPM array. Xtrim block detector module comprises of 24×24 array of 2×2×10 mm^3 crystals size and 0.05 mm $BaSO_4$ reflector which results 2.1 mm pixel pitch [15]. A 12×12 array of SiPMs with 4.2 mm pixel pitch is coupled to the crystal arrays to collect the scintillation light, thus realizing single-side readout. The key features of the Xtrim scanner are summarized in Table 1.

Experimental measurement of Xtrim performance Spatial resolution was measured using an F-18 point source in a 1 mm diameter capillary tube. An activity of 4 μCi was used with an acquisition time of 10 min for each position. The obtained projections were rebinned using Single Slice Rebinning (SSRB) rebinning method and then reconstructed using 2D ordered subsets-expectation maximization (OSEM) algorithm with 4 subsets and 5 iterations. The FWHM and full width at tenth maximum (FWTM) were determined for each extracted profile. The measured spatial resolutions were corrected for source size but were not corrected for positron range, or photon a colinearity.The same source used for spatial resolution measurement was used in experimental calculation of system sensitivity. The point source was centered in the scanner's FOV both axially and transaxially, and then stepped in 2-mm (one pixel) increments in the axial direction to both ends of the scanner, performing a 6-min scan at each position. The absolute sensitivity at each source position, determined by sum of the total counts over all the slices divided by the point source activity. The branching ratio of Na-22 (0.9060) must be taken into account as well [16].

Monte Carlo model of Xtrim: The Geant4 Application for Tomographic Emission (GATE) is a Monte Carlo (MC) simulation toolkit providing a modular, versatile and scripting language interface for instrumentation applications such as design, modeling and optimization [17]. GATE simulator is based on well-validated Geant4 libraries and allows for modeling time-dependent phenomena and moving source and detectors. In this study GATE7.2 was used to model Xtrim and our proposed PET system. An accurate geometry and model based on real Xtrim block detector size were simulated. Following the experimental sensitivity and spatial resolution measurements, performance parameters of the modeled Xtrim scanner were evaluated using various simulations. In order to validate the developed MC model, simulation results were compared with those reported experimentally obtained values (see Fig. 1).

2.2. Design and optimization

In this step, we used the validated Monte Carlo model of Xtrim to simulate a preliminarily design of brain dedicated PET scanner based on Xtrim hardware. According to geometric efficiency equation in (1) [18]:

$$\eta = \varphi \times (4\pi \sin\lfloor \tan^{-1}\left(\frac{A}{D}\right)\rfloor) \quad (1)$$

A is the scanner axial FOV and the D is ring diameter. We modeled 22 detector blocks in transaxial direction which provides 380 mm ring diameter (see Fig. 2a). Another suitable scanner model with a 20 detector blocks in a ring provides ring diameter of 34 cm with effective transaxial FOV (TFOV) of 24 cm. The larger acceptance angle increases the TFOV and system sensitivity, degrades image quality because of increase of random and scatter events, therefore an optimum angle must be calculated. One of the design requirements for our brain PET scanner is to be compatible with MRI, functional near-infrared spectroscopy (fNIRS) and Electroencephalograph (EEG) systems that are in our center. Therefore, the PET gantry should accommodate the fNIRS and EEG, and should be inserted within the available MRI system thus the PET gantry diameter is of great importance. According to Eq. (1), extending of Axial FOV (AFOV) is the best way to increase sensitivity without image quality degradation, therefore one to four block detectors modeled in axial direction providing 50.3, 105, 159 and 212 mm AFOV. Point source sensitivity calculated for each design with a given AFOV to find higher sensitivity scanner. After modeling of scanner geometry, photon detection system was simulated. Photoelectric effect, Compton, Rayleigh and multiple scattering, ionization, non-collinearity, positron range and radioactive decay are considered in our simulation whereas optical coupling between the crystals and the SiPM arrays were not modeled in this work. Light transport in the crystals were not simulated either. The modeled "digitizer" was added to simulated geometry using real Xtrim electronic data channel

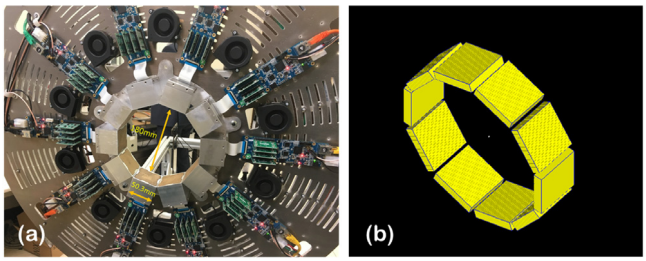

Fig. 1. (a) The view of the Xtrim animal PET scanner with 180 mm ring diameter (b). The simulated model of Xtrim using GATE MC Toolkit.

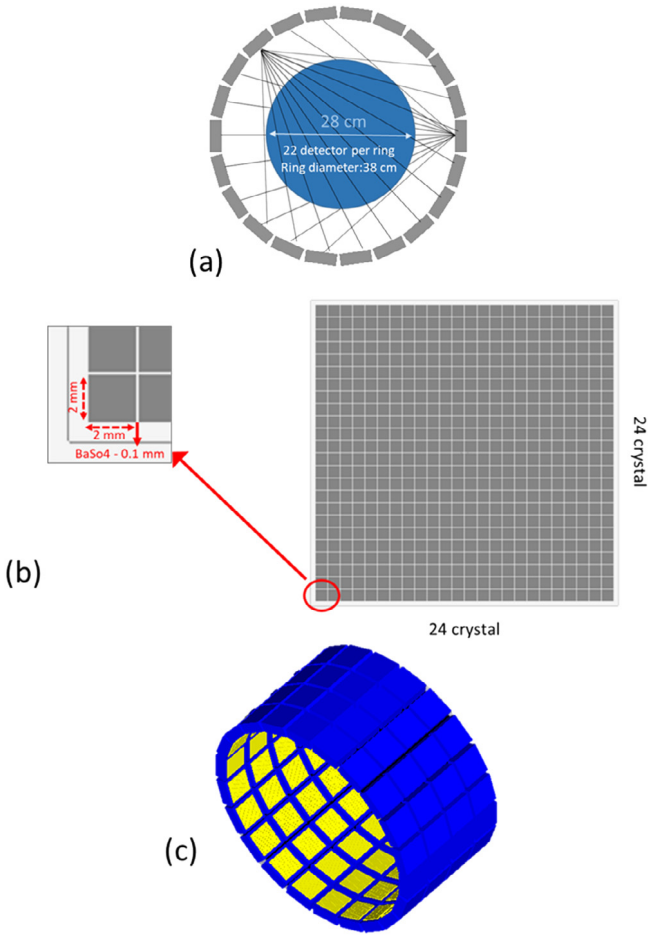

Fig. 2. (a) Illustration of the preliminary scanner geometry with given ring diameter and transaxial FOV (b) crystal array in one block detector with pixel size of 2 mm and inter-crystal gap of 0.1 mm. (c) the side view of preliminary design of brain scanner.

in GATE. A Gaussian and an exponential distribution as radioactive and system electronic noise was defined. We set the detector energy resolution to 15% FWHM in 511 keV in the energy resolution module and used 32000 photons/MeV light yield for LYSO:Ce crystal. The time resolution module was set to 1.85 ns. Two "dead-time" modules were applied: the first with a value of 600 ns (Non-paralyzable) was applied on the block level, and the second module with a value of 42 ns (paralyzable) was applied in the final electronic data collocation level. We selected energy and coincidence window based on real scanner values. We used ROOT and List Mode output to analyze the results.

After the preliminary design and modeling as a baseline configuration, we explored optimization of crystal configuration to further improve the system performance. Crystal pixel size from 2×2 to 4×4 mm^2 and crystal thickness from 10 to 30 mm were evaluated in our designed scanner with fixed block detector size. BGO, LYSO and GSO as three common scintillator materials were compared as well. Crystal pixel gaps comprised of $BaSO_4$ was fixed in 0.1 mm in all simulations (see Fig. 2b). To drive system sensitivity and spatial resolution, an F-18 point source was positioned in the center and also 10 cm offset from center to investigate photons penetration behavior. The images were reconstructed using Filtered Back projection (FBP) based on NEMA protocol . We scalarized a penta-objective function into a single objective function by the well-known weighted-sum (WS) approach which is robust to changes in relative importance factor (weight) of each objective [19].

$$\boldsymbol{Cost\,Function} = \mathbf{k}[\boldsymbol{\alpha}_1(\frac{1}{\mathbf{Sen}}) + \boldsymbol{\alpha}_2(\mathbf{FWHM}_{(0,0,0)}) + \boldsymbol{\alpha}_3(\mathbf{FWTM}_{(0,0,0)}) + \boldsymbol{\alpha}_4(\mathbf{FWHM}_{(0,10,0)}) + \boldsymbol{\alpha}_5(\mathbf{FWTM}_{(0,10,0)})] \quad (2)$$

Where K is a constant and can be set arbitrarily to 1000; α_1 to α_5 are weighting factors ($0 < \alpha_1, \alpha_2, \alpha_3, \alpha_4, \alpha_5 < 1$ and $\alpha_1 + \alpha_2 + \alpha_3 + \alpha_4 + \alpha_5 = 1$). Position-detection-accuracy (PDA) is an index of the inter-crystal scattering and penetration which highly affect the image quality. FWTM indicates better the PDA specifications than FWHM. Therefore, we added FWTM in our cost function. [19]. All parameters in proposed cost function normalized to preliminary design configuration ($2 \times 2 \times 10$ mm^3, pixel area, 0.1 mm $BaSO_4$ gap, and LYSO(Ce) crystal), respectively. In order to find optimum configuration, we devoted 0.4 value to sensitivity and 0.15 to each of FWHM and FWTM for point sources in two positions. The lowest cost value, was considered as the optimum configuration.

2.3. NEMA evaluation of BM-PET

We evaluated the performance characteristics of the optimized configuration which here we refer to Brain Mapper PET (BM-PET) (see Fig. 2c). Performance measurements are based on NEMA NU 2-2012 standard. The spatial resolution was measured using three plastic-encased 5 μCi ^{22}Na point sources with dimension of $1 \times 1 \times 1$ mm^3 and scanned for 900 s. The point sources were placed at the center and 8.5 cm from the center at axial position. For each axial position, the sources were placed at three (x, y) positions: (1 cm, 0), (0, 10 cm), and (10 cm, 0). The data was reconstructed using FBP technique. Transverse and axial spatial resolution were calculated based on fitting Gaussian function to the plotted profiles and calculating FWHM and FWTM point spread functions. Following the NEMA whole-body protocols [20], for sensitivity measurements, we simulated a 700 mm long polyethylene tube with 2 mm inner diameter filled with F-18. Five concentric aluminum tubes, each 700 mm long, five aluminum sleeves with increasing inner diameter and constant wall thickness were simulated and added to the line source [11].

2.4. Image reconstruction

After NEMA performance evaluation of the BM-PET scanner, we optimized image reconstruction algorithm. We produced sinograms from simulation results and then reconstructed them using Software for Tomographic Image Reconstruction (STIR) framework [21]. Due to lack of dedicated phantoms for brain scanners by NEMA, we simulated NEMA NU-4 Image Quality (IQ) phantom for small animal scanners inside the BM-PET for evaluation of spatial resolution, and scanned for 15 min with 18F-fluorodeoxyglucose solution of activity 3.7 MBq. This cylindrical phantom with 30 mm diameter is composed of three sections, (I) hot region with 5 five fillable rods with diameters of 1, 2, 3, 4, and 5 mm, (II) uniform section, (III) cold region with two cold chambers which are hollow cylinders with 8 mm diameter and 15 mm height. One chamber is filled with nonradioactive water, and the other is filled with air. All the datasets were reconstructed with FBP, MLEM, and OSEM reconstruction algorithms. To assess the image quality against the number of iterations in order to find optimum

iteration, the number of full iterations was evaluated from 1 to 40 and our point spread function measurements for each hot rods were computed for each iteration number. It should be noted that, 6 subsets were allocated for OSEM algorithm. CPU time calculation of each algorithms were recorded as well.

2.5. Image quality enhancement

OSEM algorithm can produce better image quality in a short computing time but the main drawback is its tendency to increase noise with increasing iterations [22]. Metz filter is one of noise-reduction and image-enhancement filters that have been used in nuclear medicine image processing that amplifies mid-range frequencies which include certain features in the underlying image [22–24]. The 1-dimensional Metz restoration filter in the frequency domain is defined as Eq. (3).

$$\mathbf{M}(\mathbf{f}) = (1 - \left(1 - [\mathbf{G}(\mathbf{f})]^2\right)^{\mathbf{N}+1})/(\mathbf{G}(\mathbf{f})) \quad (3)$$

Where N is the Metz power, f is the zero-mean Gaussian density function, $G(f)$ its transfer function ($G(0)$ defined as 1). In this section, to remedy noise artefacts and in order to regularize the system over iterations, we introduced the inter-update Metz filtered OSEM (IMF-OSEM) into the image updating process. To find optimum Metz parameters, Metz power (N) and Gaussian function FWHM ($G(f)$) were assessed from 0 to 3 and 1 to 4 in X, Y, Z directions respectively. We used NEMA-IQ phantom for quantitative analysis and modeled Derenzo phantom for qualitative evaluation of IMF-OSEM resolution recovery method.

2.6. Gap filling approach using gantry rotation

One of the major challenges to develop a high resolution PET scanner is inactive areas and large gaps between the detector modules in PET scanners which can degrade the image spatial resolution especially when analytical image reconstruction is employed. There are different methods based on in-painting approaches for compensation of produced gaps [25,26], but we believe such interpolation-based gap filling methods can degrade image quantification, therefor we used safe way based on gantry rotation to fill inter-block gaps. Rotation-mode assuming a step-and-shoot scheme using Gate simulator capabilities [27], with two angular steps to completely sweep all lines of response and increase data sampling. Scanner was rotated to half a block detector size to cover the gaps. To assess reconstructed image quality of both rotation and non-rotation mode of scanner, MicroDerenzo phantom was simulated. MicroDerenzo with hot rods of different diameters (1.5, 2, 2.5, 3, 3.5 and 4 mm), arranged into six segments. Data was reconstructed using OSEM in 6 subsets and 16 sub-iteration. In order to evaluate the resolution resolving as contrast criteria, intensity line profiles of rods were plotted. The average values of the obtained peaks and valleys were used for peak-to-valley ratio calculation. Peak-to-valley is a standard criterion to assess the resolution and image contrast [9].

2.7. Attenuation correction

The voxelized XCAT phantom was used as the digital phantom in GATE [28]. Seven homogeneous, spherical tumors of 7 mm-diameter were positioned in the end of the frontal lobe and center of the brain to evaluate small tumors quantification in center of head as an approximate criterion of quantification effect in brain. The F-18 activity ratio of the gray matter:white matter:tumor was set to 4:1:20. GATE simulation with inserted XCAT defined and inserted phantom was performed in 300 s for each tumor. The attenuation map is classified into uniform tissue classes (soft tissue (water) $0.0285 \leq I = 0.096$), three tissue classes (air ($0.0285 \geq I = 0.0$), soft tissue ($0.088 \leq I < 0.130 = 0.096$) and cortical bones ($0.130 \leq I = 0.146$)) and bilinear energy mapping [29]. In bilinear energy mapping, the attenuation map for each organs has derived from its corresponding attenuation coefficients. We used non-attenuated image as reference image. The obtained attenuated emission sinogram was corrected using STIR using the three attenuation maps (1-class, 3-class, and bilinear-class). The sinogram was reconstructed using OSEM (6 subset, 16 sub-iteration) algorithm to provide the corrected PET image. ROI was plotted for each tumor compared to the reference image. A mean relative error was obtained for each tumor using Eq. (4), where a negative relative error indicates that the corrected image underestimates the initial activity, whereas a positive relative error indicates overestimation of the original activity map.

$$Relative\ Error(\%) = \frac{Measured\ activity - Original\ activity}{original\ actvity} \times 100 \quad (4)$$

2.8. Brain phantom imaging

For image quality evaluation and to mimic activity distribution in brain imaging, 3D Hoffman brain phantom inside BM-PET were simulated [30]. The modeled Hoffman phantom comprised of 19 slices with an image matrix size 196 ×196 and a voxel size of 1.25 ×1.25×10 mm^3. The tracer was F-18 and the activity ratio of the gray matter:white matter:cerebrospinal fluid (CSF) was set to 5:1:0. The attenuation image in each slice was uniform with an attenuation coefficient of 0.0095 mm^{-1}. Simulation was performed for 30 min scan time. Scatter estimation of simulated phantom was extracted in Gate sinogram output and obtained image was corrected for attenuation using STIR pre-reconstruction correction method based on water attenuation correction factors. All output data was reconstructed using optimized reconstruction algorithm and Metz filter parameters. Reconstructed image with and without corrections and resolution recovery method were compared together using intensity profile plotting.

3. Results

3.1. Validation and verification results

Xtrim's experimental and simulation results of radial, tangential and axial FWHM and FWTM for point source at three different positions as defined in the NEMA NU-4 2008 standard is reported in Table 2. Experimental and simulation values for system sensitivity are 1.56%, and 1.63%, respectively showing good agreement. Validation study of Xtrim Gate MC Model indicated that difference between experimental measurements and simulation results for resolution and sensitivity is smaller than ~10%, paving the way for GATE-based design and optimization of the BM-PET.

3.2. Design and optimization results

Based on analytical calculation, 34-cm-diameter scanner achieved higher sensitivity than 38-cm-diameter scanner, but provides higher parallax errors, for instance for point source positioned in 12 cm of center of FOV (CFOV), parallax error value will be 1.17 times higher than 38-cm-diameter scanner. Non-collinearity of annihilation photons depends on ring diameter (D) can affects on system spatial resolution by $(0.0022\Delta D)^2$ factor in mm which is negligible for ΔD = 4 cm. Therefore, to accommodate fNIRS and EEG equipment inside the PET scanner, smaller acceptance angle along with adequate TFOV to coverage of all head sizes and lower parallax error, we choose 38-cm-diameter model for our scanner design. Simulated point source sensitivity for the PET scanner with 50.3, 105, 159 and 212 mm long AFOV is 0.6%, 1.7%, 3.0% and 4.1%, respectively. The results indicated that for 38-cm-diameter scanner based on Xtrim detector blocks, higher sensitivity achieved by 212 mm axial length.

In crystal size optimization, we evaluated the effect of crystal thickness on the percentage of scanners' sensitivity. We observe that increase in crystal thickness from 10 mm to 30 mm, sensitivity significantly raised from 4% to 13%. Results indicated that spatial resolution for

Table 2
Spatial resolution comparison between experimental and simulation result.

Spatial resolution	Radial displacement 5 m			Radial displacement 10 mm			Radial displacement 15 mm		
	Radial	Tang	Axial	Radial	Tang	Axial	Radial	Tang	Axial
FWHM(Experimental)	1.6	1.7	1.8	1.9	1.7	2.1	1.9	1.8	2.3
FWHM(Simulation)	1.5	1.6	1.7	1.8	1.8	2	1.9	1.9	2.1
Difference	6.2%	5.8%	5.5%	5.2%	5.8%	4.7%	0%	5.5%	8.6%
FWTM(Experimental)	3.5	3.6	3.7	3.8	3.6	4.1	3.9	3.8	4.5
FWTM(Simulation)	3.1	3.2	3.3	3.4	3.5	3.8	3.7	3.6	4.1
Difference	11.4%	11.1%	10.8%	10.5%	2.7%	7.3%	5.1%	5.2%	8.8%

Table 3
Comparison of different crystal size configurations in the confined block detector size based on their ranks obtained by Eq. (2). The lowest cost function, was considered as the optimum crystal configuration.

Crystal size(mm)	Normalized sensitivity (%)	Normalized FWHM (mm) $R = 0$	Normalized FWHM (mm) $R = 10$	Normalized FWTM (mm) $R = 0$	Normalized FWTM (mm) $R = 10$	Cost function
$2 \times 2 \times 10$	1	1	1	1	1	1000
$2 \times 2 \times 20$	2.39	1.03	1.02	1.03	1.01	780
$2 \times 2 \times 30$	3.34	1.08	1.39	1.08	1.40	862
$3 \times 3 \times 10$	1.01	1.42	1.30	1.35	1.30	1202
$3 \times 3 \times 20$	2.43	1.43	1.37	1.42	1.37	1003
$3 \times 3 \times 30$	3.38	1.44	1.71	1.43	1.70	1060
$4 \times 4 \times 10$	1.02	1.81	1.39	1.81	1.39	1352
$4 \times 4 \times 20$	2.45	1.84	1.57	1.84	1.57	1186
$4 \times 4 \times 30$	3.41	1.88	1.98	1.88	1.94	1269

point source at center and 10-cm off center in terms of FWHM and FWTM is a function of pixel size and as expected resolution worsens with larger pixel size. Cost function for various crystal size and detector configurations is shown in Table 3. Obtained cost function values indicated that crystal size of $2 \times 2 \times 20$ mm^3 has the lowest value (optimum solution). Crystal material evaluation showed that BGO-to-LYSO system sensitivity was 1.21 (11.8% against 9.8%) and GSO-to-LYSO was 0.74 (7% against 9.8%). Obtained mean FWHM spatial resolution for point source in center and 10-cm off-center for BGO, LYSO and GSO was 3.75, 3.05, and 3.01 mm, respectively. Mean FWTM spatial resolution for the same crystal types was 7.42, 6.07, and 6.12, respectively. After calculation of scintillators cost function by devoting of 0.4 for sensitivity and 0.6 for spatial resolution based on Eq. (2), we arrived at 1000, 1165 and 1048 values for LYSO, GSO and BGO showing that LYSO is the better candidate.

3.3. BM-PET NEMA results

The mean FWHM transverse and axial spatial resolution for the simulated point source in radial position of 1 cm were measured at 2.4 and 2.9 mm whereas these values for 10 cm off-center were 4.6 and 3.3 mm. Simulated sensitivity values as a function of accumulated sleeve thickness for the BM-PET was 16 cps/kBq and 18 cps/kBq for center and 10-cm off center respectively.

3.4. Image reconstruction

Fig. 3 shows the central slice of the reconstructed images of the NEMA NU-4 IQ phantom by the three reconstruction approaches introduced earlier at different numbers of full iterations. It can be seen that MLEM and OSEM can reach better images than FBP. It should be noted that the 1-mm hot rod cannot be seen in figures by our scanner.

FWHM values for hot rods showed the best iteration number for OSEM and MLEM algorithms occurs at sixteen. Recorded computing (until convergence) time for OSEM was 5 times faster than that of MLEM, therefore OSEM with 6 subsets and 16 sub-iterations was selected as optimum reconstruction parameters.

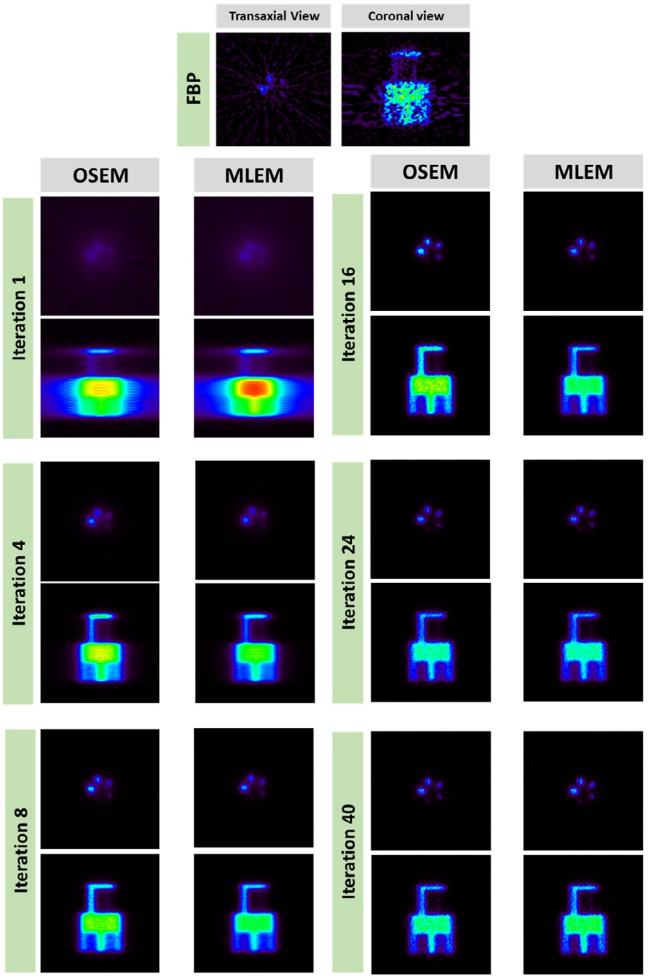

Fig. 3. Sample slices of NEMA-NU 2008 IQ phantom by different reconstruction algorithm and different iteration in transaxial and coronal views.

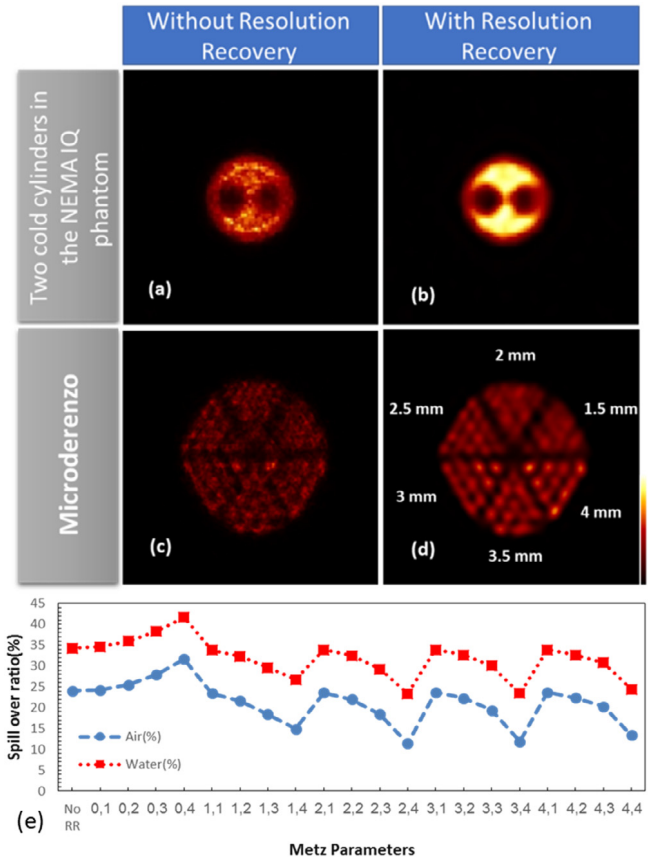

Fig. 4. Reconstructed images of (a) NEMA IQ phantom without resolution recovery (b) NEMA IQ phantom with resolution recovery (c) Microderenzo phantom without resolution recovery (d) Microderenzo phantom with resolution recovery. (e) Calculated SOR for both air and water cylinders in NEMA IQ phantoms based on Metz filter parameters.

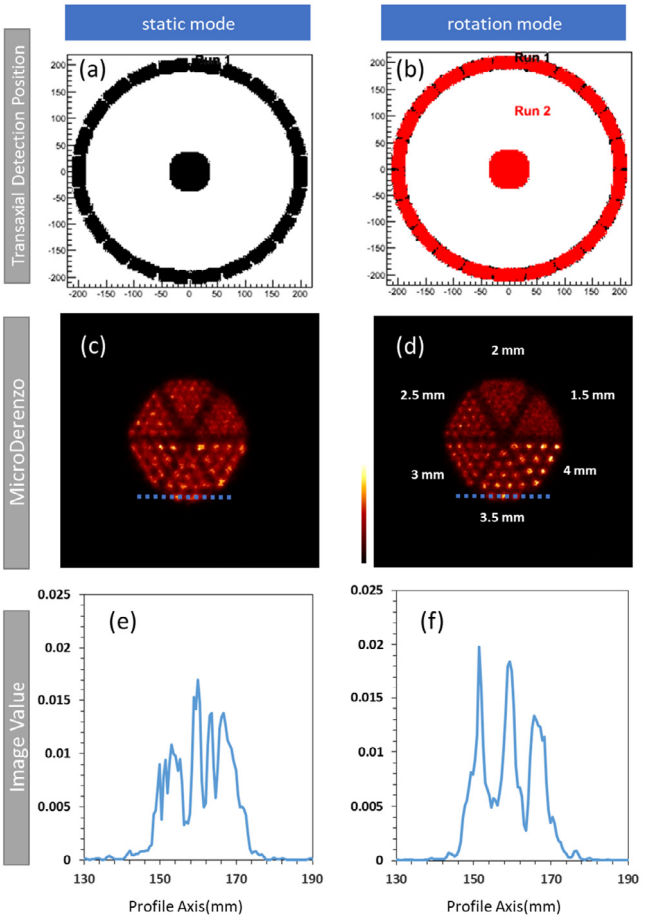

Fig. 5. Transaxial detection position of annihilation photons in BM-PET in (a) static mode (b) rotation mode. Reconstructed image of Micro-Derenzo phantom in (c) static mode (d) rotation mode.

3.5. Image enhancement results

The two air and water filled cylinders as cold regions was quantized as spillover ratio (or the cold-air – and water – SORair and SORwat), for a cylindrical volume of interest (VOI) using Eq. (5). The VOI was considered such that it surrounds central part of each cold phantom with diameter of 4 mm and encompassed the central 7.5 mm in length.

$$SOR = \frac{Mean\ activity\ in\ VOI}{Mean\ Background\ activity} \quad (5)$$

Fig. 4 Show SOR values as a function of Metz parameters. The Metz power of 2 and Gaussian function FWHM of 4 could provide lowest SOR for both air and water cylinders. Averaged SOR for the two air-filled cold cylindrical regions of the NEMA IQ phantom was calculated with 13% improvement with optimum Metz filter parameters. Reconstructed image of the MicroDerenzo phantom with and without resolution recovery (see Fig. 4) indicates that optimized IMF-OSEM can provide near noise-free and high contrast images compared with the image without resolution recovery.

3.6. Gantry rotation results

Transaxial position of the detected photons as well as in the MicroDerenzo phantom images in both static and rotation mode are shown in Fig. 5(a, b). We observe that in rotation mode, as expected, inter-block gaps between detectors is covered leading to adequate sampling (Fig. 5b). Furthermore, the transverse spatial resolution based on NEMA, was improved from 2.4 in static mode to 2.1 in rotation mode.

One center slice of MicroDerenzo phantom was compared for rotation and static mode (see Fig. 5(c, d). In the rotation mode (Fig. 5d) one can observe an artifact-free high image quality in terms of spatial resolution and contrast compared with that of the static mode (Fig. 5c). Unlike in static mode, 2.5-mm diameter hot rods are clearly resolved. By plotting a profile intensity across one row of the 3.5-mm rods, we observe that rods are not completely resolved in the static data acquisition mode in that an additional peak in the intensity profile (see Fig. 5e) was observed as a result of cross-contamination between adjacent voxels. As expected, the peak-to-valley as contrast criterion is improved in rotating image acquisition mode in Fig. 5f compared to that of Fig. 5e.

3.7. Attenuation correction

Fig. 6 illustrates the statistical analysis of the relative error for different tumors based on different attenuation correction of the XCAT phantom. The obtained results substantiates the hypothesis that the higher the number of tissue classes in the attenuation map, the more the recovered activity approaches the original activity for lesions located in the brain. When using the uniform attenuation map, the median relative error is equal to −8.4% and for three class attenuation map, the value is equal to −1.5%. Without attenuation correction, the relative error increases to −15.7%. It should be noted that, to counteract the scatter effect in the obtained results, all estimated scatter sinograms

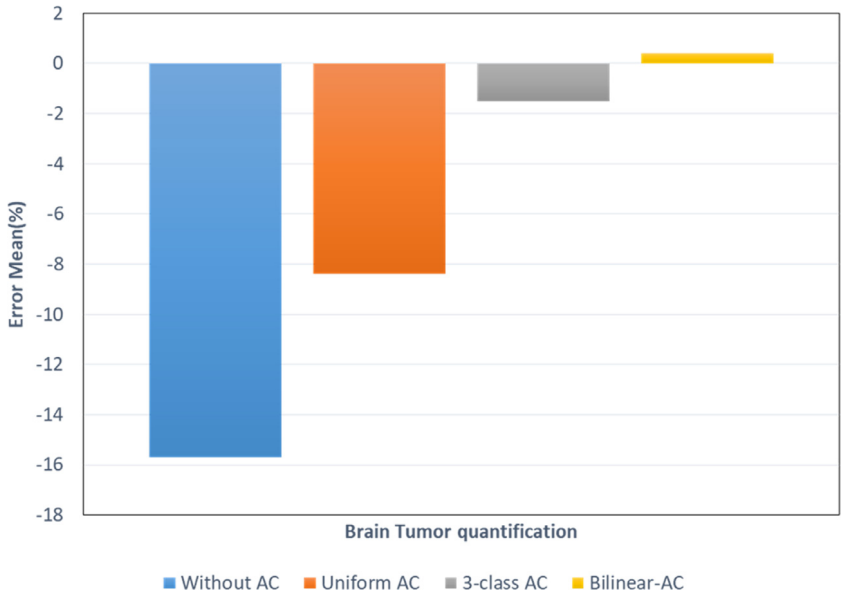

Fig. 6. Average relative error mean for lesions inside brain for the XCAT phantom inside the BM-PET scanner with different attenuation correction methods.

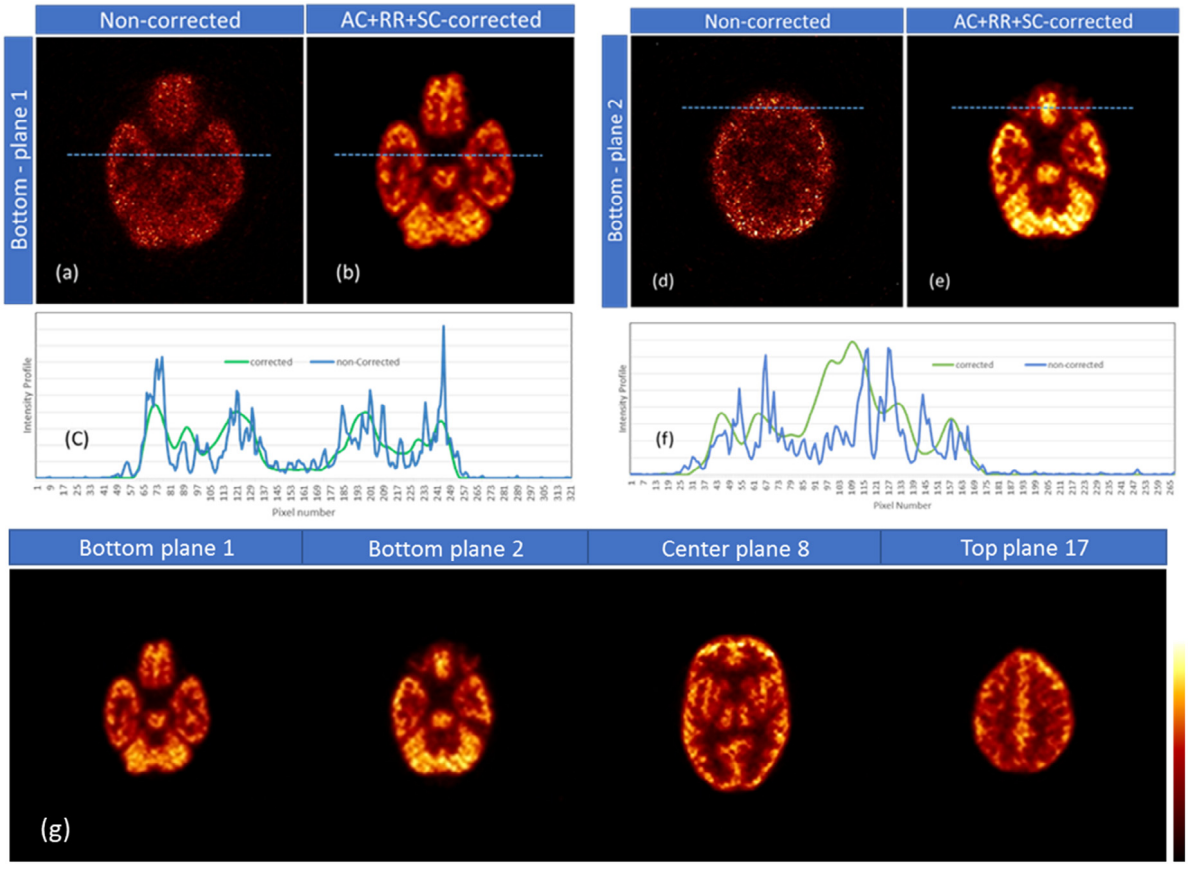

Fig. 7. ^{18}F-FDG brain images acquired with the BM-PET scanner along with plotted intensity profiles through images. A clear improvement in contrast and image quality and noise reduction can be observed using attenuation and scatter correction, and resolution recovery (a–f). ^{18}F-FDG brain images in different planes acquired with the BM-PET scanner (g).

subtracted from original sinogram to only evaluate the attenuation and its correction effect in brain images. The results showed that without attenuation correction, tumor quantification in BM-PET scanner will be challenging, and therefore, at least a simple attenuation correction method should be implemented to recover the original activity.

3.8. Brain phantom imaging results

Fig. 7 compares top, middle and bottom slices of the Hoffman phantom reconstructed images using OSEM algorithm (6 subset, 16 sub iteration) with and without attenuation correction (AC), scatter

Table 4
(a) Comparison of simulated effective transaxial FWHM resolution with respect to the scanners' crystal size for BM-PET, ECAT-HRRT and NeuroPET. (b) Comparison of system sensitivity with respect to the scanner ring diameter, axial length, and total used crystal volume of the same scanners.

(a) System	Crystal size	Transaxial FWHM resolution at 10 mm (mm)	Resolution/crystal size
NeuroPET/CT	2.3	2.9	1.26
ECAT-HRRT [1]	2.1	2.3	1.45
BM-PET(Static-mode)	2	2.4	1.2
BM-PET(Rotation-mode)	2	2.1	1.05

(b) System	Ring diameter (mm)	Axial length (cm)	Total used crystal volume (cm3)	Point source sensitivity in CFOV (%)	$\frac{Sensitivity}{Totalcrystalvolume}(\times 10^4)$
ECAT-HRRT-Siemens	469	253.5	5284 (LYSO-LSO)	3.3–4.7	6.2–8.9
NeuroPET/CT	357	220	2778 (LYSO)	≈8.2	29
BM-PET (Static-mode)	380	212	4055(LYSO)	9.8	24.2
BM-PET (Rotation-mode)	380	212	4055(LYSO)	9.8	24.2

correction (SC) and resolution recovery (RR). As expected, high quality image with low noise and high contrast was produced when all three corrections (AC+SC+RR) were used (see Fig. 7). In non-corrected images, many details cannot be resolved, intensity in surrounding regions of brain is higher than central regions due to attenuation, and images are noisy and low contrast due to scatters and inherent noise artifacts.

Discussion and conclusion

The BM-PET project is under development and the presented results in this paper are based on Monte Carlo simulation study. We designed, modeled, optimized and evaluated rotating cylindrical MR-compatible brain PET in GATE environment based on expanding the geometry of our recently developed small animal PET system, the Xtrim PET. Using the Xtrim model as a building block provided a suitable platform for design and performance evaluation of the BM-PET under development at our center. The BM-PET design is based on long axial FOV that facilitates acquiring a brain image in one bed position.

Comparison results of BGO and LYSO showed that BGO achieves higher sensitivity than LYSO due to its higher Z and rather higher photo-fraction, however, better energy and time resolution of LYSO allows tight energy and time windowing which makes improvement in spatial resolution and image quality [31]. The GATE obtained sensitivity results provided comparable results with analytical calculations. Intrinsic detection efficiency of a crystal in analytical calculation, in the simplest terms, is proportional to 1-exp $(-\mu_{ph}t)$, where μ_{ph} is photoelectric linear attenuation coefficient of the crystal and t is crystal thickness [32]. We obtained 1.03 for analytical calculation of LYSO-to-BGO efficiency which has good agreement with our simulations (1.2) presented in Table 4b. The low obtained difference may arise from different energy window settings for LYSO and BGO. BGO is cheaper than LYSO and achieve higher sensitivity and delivered almost same cost function, but our simulation does not include high activities and evaluate the effects due to pulse pileup which lead to a degradation of scatter fraction and spatial resolution which is less significant for LYSO thanks to its faster decay constant.

In this study, we only evaluated the effect of gantry rotation on image quality, and rotation optimization was not performed. "Step and Shoot" method for rotation was applied and due to small needed angle, only one rotation was selected. Visual inspection of the MicroDerenzo phantom images indicated that the rotation mode improved the spatial resolution, hot rods resolving, and image contrast. These improvements are clearly shown on the intensity profiles for each scan. Increase of the sampling density by rotation mechanism is the key factor of image quality improvement.

We have shown that attenuation corrections are important for small diameter tumors in XCAT phantom. Both ROI analysis on the reconstructed images showed that, regardless of the method and classes used, correction for attenuation is necessary for the quantitative accuracy. Although uniform water AC which was approximated by a uniform region inside the head border delivers about 8% quantitative error but it yielded improved quantitation of ~7%. Given that our ultimate goal is to integrate the BM-PET with a MRI scanner, attenuation map will be extracted from MRI scans for improved accuracy. It has been shown that ultra-short echo-time (UTE) MRI sequences can differentiate bone from air [33,34]. In another approach, using short echo-time (STE) in combination with long echo-time (LTE) resulted in even better differentiation of bone from air cavities in the head area [35]. Therefore, MR based attenuation map produced by mentioned sequences using 3-class can provide more accurate results and quantification errors can be reduced to below 2%. Also, the high contrast anatomical MR brain images in addition to the attenuation correction increase diagnostic accuracy when combined with brain PET images. Scatter and attenuation correction along with resolution recovery simultaneously improved our image quality.

While we are aware that results from modeled scanners in GATE can be different from a manufactured scanner, we evaluated our comparisons with simulated models of the existing brain-dedicated PET systems. For example, an accurate GATE model for NeuroPET scanner presented by us in [11] and then we use this model findings to compare data. Table 4a compares the transaxial spatial resolution obtained from a point source at 10-mm radial offset from BM-PET in both static and rotating modes along with those of the NeuroPET and ECAT-HRRT scanners. BM-PET can provide lowest spatial resolution than other scanners because of small crystal size and delivers comparable results against other scanners. Results show that rotation-mode for BM-PET improves spatial resolution due to increase of data sampling and inter detector gap filling. According to Fig. 3 in 16 iteration, The BM-PET have capability of to detect down to 2-mm-diameter hot rods without background activity. Such a good spatial resolution is achievable by small pre-clinical PET scanners.

Table 4b indicates the values of system sensitivity for each simulated scanner. As expected, the affecting factors in sensitivity is the solid-angle coverage that can be obtained by small ring diameter and long axial FOV. The ECAT scanner ring is larger than currently available brain PETs and especially BM-PET, therefore its sensitivity is lower than BM-PET. Ring diameter and axial FOV in NeuroPET is almost same with BM-PET scanner, but BM-PET provides higher sensitivity. In this study we presented total used crystal volume as an advantageous parameter to evaluate system sensitivity and system manufacturing cost. Total crystal volume is directly proportional to sensitivity and a larger detector coverage along with the smaller ring diameter leads to higher sensitivity. In the results we showed that 16 cps/kBq sensitivity and spatial resolution of 2.1 mm is achievable. Future work will examine the effect of the adding time-of-flight and depth-of-interaction information on BM-PET performance.

Acknowledgments

This work was supported under grant number 30847, Tehran University of Medical Sciences, Tehran, Iran.

References

[1] H.W. de Jong, F.H. van Velden, R.W. Kloet, F.L. Buijs, R. Boellaard, A.A. Lammertsma, Performance evaluation of the ECAT HRRT: an LSO-LYSO double layer high resolution, high sensitivity scanner, Phys. Med. Biol. 52 (2007) 1505.
[2] K.J. Hong, Y. Choi, J.H. Jung, J. Kang, W. Hu, H.K. Lim, Y. Huh, S. Kim, J.W. Jung, K.B. Kim, A prototype MR insertable brain PET using tileable GAPD arrays, Med. Phys. 40 (2013).
[3] S. Yamamoto, M. Honda, T. Oohashi, K. Shimizu, M. Senda, Development of a brain PET system, PET-Hat: a wearable PET system for brain research, IEEE Trans. Nucl. Sci. 58 (2011) 668–673.
[4] P. Sheikhzadeh, H. Sabet, H. Ghadiri, P. Geramifar, P. Ghafarian, M. Ay, Concept design and Monte Carlo performance evaluation of HeadphonePET: a novel brain-dedicated PET system based on partial cylindrical detectors, J. Instrum. 13 (2018) P07008.
[5] H. Tashima, T. Yamaya, Proposed helmet PET geometries with add-on detectors for high sensitivity brain imaging, Phys. Med. Biol. 61 (2016) 7205.
[6] P. Sheikhzadeh, H. Ghadiri, P. Geramifar, P. Ghafarian, M.R. Ay, Design and performance evaluation of spheroid geometry for brain PET scanner using Monte Carlo modeling, Iran. J. Nucl. Med. 27 (2019) 32–38.
[7] K. Gong, S. Majewski, P.E. Kinahan, R.L. Harrison, B.F. Elston, R. Manjeshwar, S. Dolinsky, A.V. Stolin, J.A. Brefczynski-Lewis, J. Qi, Designing a compact high performance brain PET scanner—simulation study, Phys. Med. Biol. 61 (2016) 3681.
[8] H. Herzog, K.-J. Langen, C. Weirich, E.R. Kops, J. Kaffanke, L. Tellmann, J. Scheins, I. Neuner, G. Stoffels, K. Fischer, High resolution BrainPET combined with simultaneous MRI, Nuklearmedizin 50 (2011) 74–82.
[9] J.Y. Suk, C.J. Thompson, A. Labuda, A.L. Goertzen, Improvement of the spatial resolution of the MicroPET R4 scanner by wobbling the bed, Med. Phys. 35 (2008) 1223–1231.
[10] K. Grogg, T. Toole, J. Ouyang, X. Zhu, M.M. Normandin, K. Johnson, N.M. Alpert, G. El Fakhri, NEMA and clinical evaluation of a novel brain PET-CT scanner, J. Nucl. Med. (2015) jnumed. 115159723.
[11] P. Sheikhzadeh, H. Sabet, H. Ghadiri, P. Geramifar, H. Mahani, P. Ghafarian, M.R. Ay, Development and validation of an accurate GATE model for NeuroPET scanner, Phys. Med. (2017).
[12] K.J. Hong, Y. Choi, J.H. Jung, J. Kang, W. Hu, H.K. Lim, Y. Huh, S. Kim, J.W. Jung, K.B. Kim, MR insertable brain PET using tileable GAPD arrays, in: Nuclear Science Symposium Conference Record (NSS/MIC), 2010 IEEE, IEEE, 2010, pp. 2016–2019.
[13] G. Sportelli, S. Ahmad, N. Belcari, M.G. Bisogni, N. Camarlinghi, A. Di Pasquale, S. Dussoni, J. Fleury, M. Morrocchi, E. Zaccaro, The TRIMAGE PET data acquisition system: initial results, IEEE Trans. Radiat. Plasma Med. Sci. 1 (2017) 168–177.
[14] A. Del Guerra, S. Ahmad, M. Avram, N. Belcari, A. Berneking, L. Biagi, M.G. Bisogni, F. Brandl, J. Cabello, N. Camarlinghi, TRIMAGE: A dedicated trimodality (PET/MR/EEG) imaging tool for schizophrenia, Eur. Psychiatry 50 (2018) 7–20.
[15] S. Sajedi, N. Zeraatkar, M. Taheri, S. Kaviani, H. Khanmohammadi, S. Sarkar, H. Sabet, M.R. Ay, Generic high resolution PET detector block using 12× 12 SiPM array, Biomed. Phys. Eng. Express 4 (2018) 035014.
[16] N. Zeraatkar, M.R. Ay, A. Kamali-Asl, H. Zaidi, Accurate Monte Carlo modeling and performance assessment of the X-PET™ subsystem of the FLEX Triumph™ preclinical PET/CT scanner, Med. Phys. 38 (2011) 1217–1225.
[17] S. Jan, G. Santin, D. Strul, S. Staelens, K. Assie, D. Autret, S. Avner, R. Barbier, M. Bardies, P. Bloomfield, GATE: a simulation toolkit for PET and SPECT, Phys. Med. Biol. 49 (2004) 4543.
[18] S.R. Cherry, M. Dahlbom, PET: physics, instrumentation, and scanners, in: PET, Springer, 2006, pp. 1–117.
[19] H. Mahani, G. Raisali, A. Kamali-Asl, M.R. Ay, Monte Carlo optimization of crystal configuration for pixelated molecular SPECT scanners, Nucl. Instrum. Methods Phys. Res. A 844 (2017) 1–6.
[20] N.E.M. Association, NEMA standards publication NU 2-2007: performance measurements of positron emission tomographs, National Electrical Manufacturers Association, 2007.
[21] K. Thielemans, C. Tsoumpas, S. Mustafovic, T. Beisel, P. Aguiar, N. Dikaios, M.W. Jacobson, STIR: software for tomographic image reconstruction release 2, Phys. Med. Biol. 57 (2012) 867.
[22] M. Jacobson, R. Levkovitz, A. Ben-Tal, K. Thielemans, T. Spinks, D. Belluzzo, E. Pagani, V. Bettinardi, M. Gilardi, A. Zverovich, Enhanced 3D PET OSEM reconstruction using inter-update Metz filtering, Phys. Med. Biol. 45 (2000) 2417.
[23] M. Sadki, M.T. San-Martin, Inter-update Metz filtering as regularization for variable block-ART in PET reconstruction, Computational Imaging III, Int. Soc. Opt. Photonics (2005) 394–404.
[24] M. Lyra, A. Ploussi, Filtering in SPECT image reconstruction, J. Biomed. Imaging 2011 (2011) 10.
[25] U. Tuna, S. Peltonen, U. Ruotsalainen, Gap-filling for the high-resolution PET sinograms with a dedicated DCT-domain filter, IEEE Trans. Med. Imaging 29 (2010) 830–839.
[26] C.T. Shih, J. Wu, H.H. Lin, S.J. Chang, K.S. Chuang, A novel adaptive discrete cosine transform-domain filter for gap-inpainting of high resolution PET scanners, Med. Phys. 41 (2014).
[27] M. Rodríguez-Villafuerte, Y. Yang, S.R. Cherry, A Monte Carlo investigation of the spatial resolution performance of a small-animal PET scanner designed for mouse brain imaging studies, Phys. Medica 30 (2014) 76–85.
[28] W. Segars, G. Sturgeon, S. Mendonca, J. Grimes, B.M. Tsui, 4D XCAT phantom for multimodality imaging research, Med. Phys. 37 (2010) 4902–4915.
[29] A. Akbarzadeh, M.R. Ay, A. Ahmadian, N.R. Alam, H. Zaidi, MRI-guided attenuation correction in whole-body PET/MR: assessment of the effect of bone attenuation, Ann. Nucl. Med. 27 (2013) 152–162.
[30] E. Hoffman, P. Cutler, W. Digby, J. Mazziotta, 3-D phantom to simulate cerebral blood flow and metabolic images for PET, IEEE Trans. Nucl. Sci. 37 (1990) 616–620.
[31] M. Berger, J. Hubbell, S. Seltzer, J. Chang, J. Coursey, R. Sukumar, D. Zucker, XCOM: photon cross sections database, 1998, http://www.physics.nist.gov/PhysRefData/Xcom/Text,XCOM.html.
[32] G.F. Knoll, Radiation Detection and Measurement, John Wiley & Sons, 2010.
[33] V. Keereman, Y. Fierens, T. Broux, Y. De Deene, M. Lonneux, S. Vandenberghe, MRI-based attenuation correction for PET/MRI using ultrashort echo time sequences, J. Nucl. Med. 51 (2010) 812–818.
[34] C. Catana, A. van der Kouwe, T. Benner, C.J. Michel, M. Hamm, M. Fenchel, B. Fischl, B. Rosen, M. Schmand, A.G. Sorensen, Toward implementing an MRI-based PET attenuation-correction method for neurologic studies on the MR-PET brain prototype, J. Nucl. Med. 51 (2010) 1431–1438.
[35] P. Khateri, H.S. Rad, A. Fathi, M.R. Ay, Generation of attenuation map for MR-based attenuation correction of PET data in the head area employing 3D short echo time MR imaging, Nucl. Instrum. Methods Phys. Res. A 702 (2013) 133–136.